Electronic Supplementary Material (ESI) for RSC Advances.

Supplementary Information

La_2O_3-coated $Li_2ZnTi_3O_8$@C as a high performance anode for lithium-ion batteries

Zhaohui Meng [a], Suhong Wang [a], Hongwei Wang [a], Lijuan Wang [a, *] and Song Wang [b, *]

[a] College of Chemistry and Pharmaceutical Engineering, Nanyang Normal University, Nanyang 473061, Henan, China; [b] School of Chemistry and Material Science, Liaoning Shihua University, Fushun 113001, Liaoning, China.

*Corresponding author:

Mrs. Lijuan Wang

School of Chemistry and Material Science, Liaoning Shihua University, Fushun 113001, Liaoning, China;

E-mail address: lijuanw123@163.com

Tel.: +8624-56861711

Experimental

Physical characterization and electrochemical measurements

Carbon content analysis was conducted on a RD496 thermal analyzer from room temperature to 700 °C in air. The phases were investigated via an X-ray diffraction technique conducted on a Bruker D8 Advance X-ray diffractometer with Cu Kα radiation (λ = 1.54 Å) in the 2θ ranges of 5-85 °. The morphologies of the products were observed by SU8220 scanning electron microscopes (SEM). The high-resolution transmission electron microscope (HRTEM) (FEI Tecnai F20) was used to observe the nanoscale microstructures. The specific surface areas and pore size distributions were measured via N_2 adsorption on a specific surface area and pore size distribution analyzer (3H-2000PS2). X-ray photoelectron spectroscopy (XPS) measurements (PHI 5600 CI, mono-chromatic Al-Ka radiation) were used to identify the surface species. The mass fraction of La in the final product was calculated from elemental analysis by ICP (Inductive Coupled Plasma Emission Spectrometer, PerkinElmer Optima 8000) measurement.

The electrochemical measurements were performed in CR2025 coin-type cells. The working electrode was composed of 85 wt.% active material for LZTO@C@La_2O_3 or LZTO@C, 10 wt.% conductive agent of acetylene black, and 5 wt.% binder of polyvinylidene difluoride (PVDF). The assembly of the cells was carried out in a glove box filled with high purity argon. Charge-discharge and cyclic voltammetry (CV) measurements were in the range of 0.02-3.0 V. The specific capacities of $Li_2ZnTi_3O_8$@C and $Li_2ZnTi_3O_8$@C@La_2O_3 are based on the mass of

$Li_2ZnTi_3O_8$@C and $Li_2ZnTi_3O_8$@C@La_2O_3, respectively. Electrochemical impedance spectroscopies (EIS) were recorded with an *ac* voltage of 5 mV from 10 mHz to 100 kHz. The coin-type cells after cycling were transferred to a glove box and then dissembled. The LZTO@C@La_2O_3 and LZTO@C electrodes were rinsed using dimethyl carbonate (DMC) to remove the electrolyte from the electrode surface. Then, electrodes were dried in the glove box antechamber to remove the residual DMC. The morphologies of the LZTO@C@La_2O_3 and LZTO@C electrodes before and after cycling were observed by S4800 scanning electron microscopes.

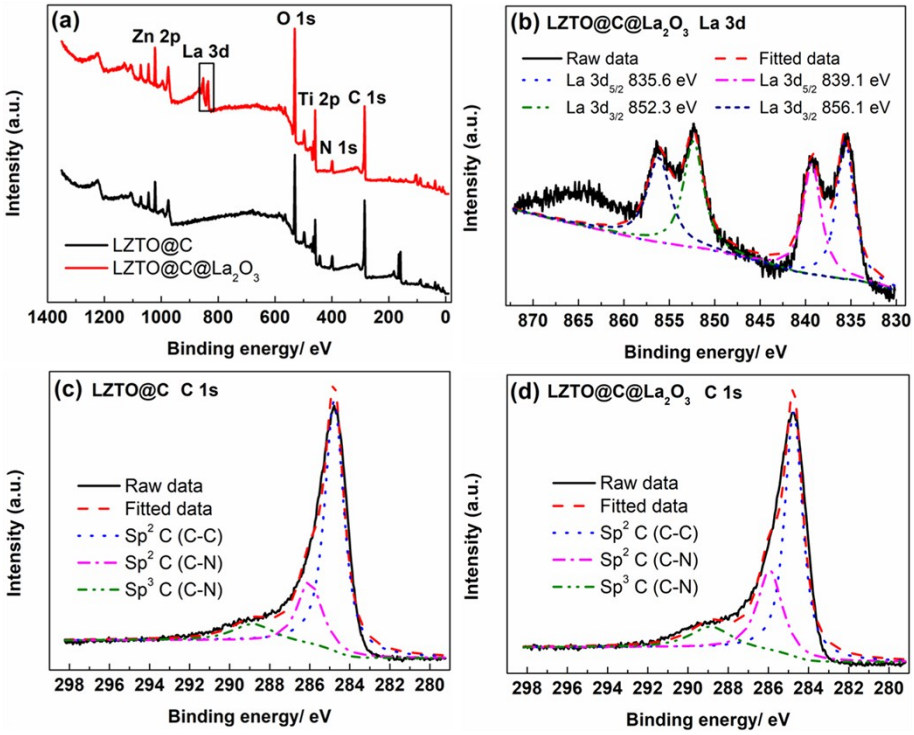

Fig. S1 (a) XPS spectra of LZTO@C and LZTO@C@La_2O_3; (b) High-resolution La 3d XPS spectrum of LZTO@C@La_2O_3; High-resolution C 1s XPS spectra of (c) LZTO@C and (d) LZTO@C@La_2O_3.

The XPS spectra of LZTO@C and LZTO@C@La_2O_3 are shown in Fig. S1a. It can be seen that Zn, Ti, O, C and N exist in LZTO@C and LZTO@C@La_2O_3. In

addition, there is La element in LZTO@C@La_2O_3, corresponding to the two peaks from 831 to 859 eV, attributed to the two spin orbits of La $3d_{5/2}$ and La $3d_{3/2}$, respectively [S1]. The high-resolution XPS spectrum of La 3d are depicted in Fig. S1b. The values of binding energy are in good line with the La 3d in La_2O_3 [S1], indicating that the La element in the form of La_2O_3 exists in LZTO@C@La_2O_3. The high-resolution XPS spectra of C 1s for LZTO@C and LZTO@C@La_2O_3 anodes (Fig. S1c-d) can be fitted into three types of C contributions, i.e., sp^2 C (C-C) about 284.8 eV, sp^2 C (C-N) about 286 eV and sp^3 C (C-N) at 288.8 eV.

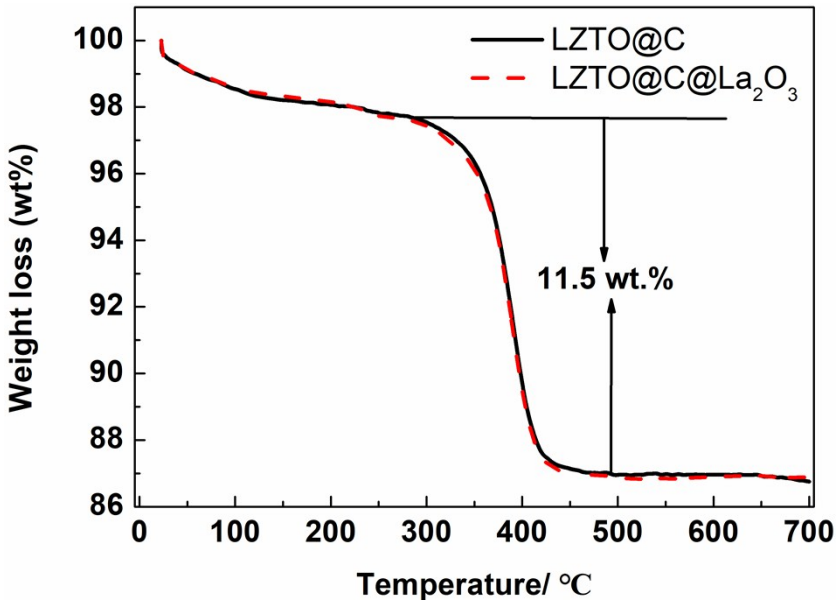

Fig. S2 TG curves of LZTO@C and LZTO@C@La_2O_3.

The carbon content in LZTO@C and LZTO@C@La_2O_3 quantified by TG measurement is shown in Fig. S2. It can be seen that the slow weight loss from room temperature to 200 °C may be attributed to the evaporation of adsorbed water (2.0 wt.%) from the composites. The oxidation of carbon in air occurs from 300 to 450 °C with sharp weight loss. The carbon content is ca. 11.5 wt.% for the two samples.

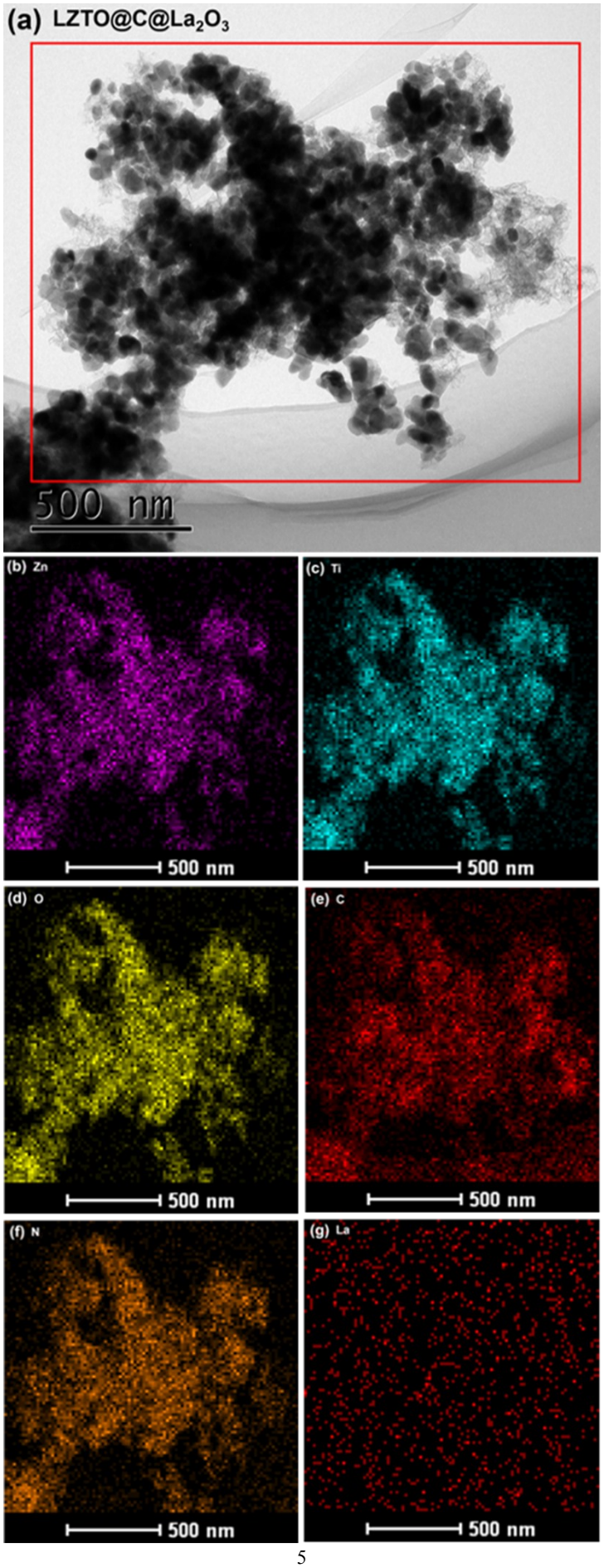
(a) LZTO@C@La2O3
500 nm
(b) Zn
500 nm
(c) Ti
500 nm
(d) O
500 nm
(e) C
500 nm
(f) N
500 nm
(g) La
500 nm

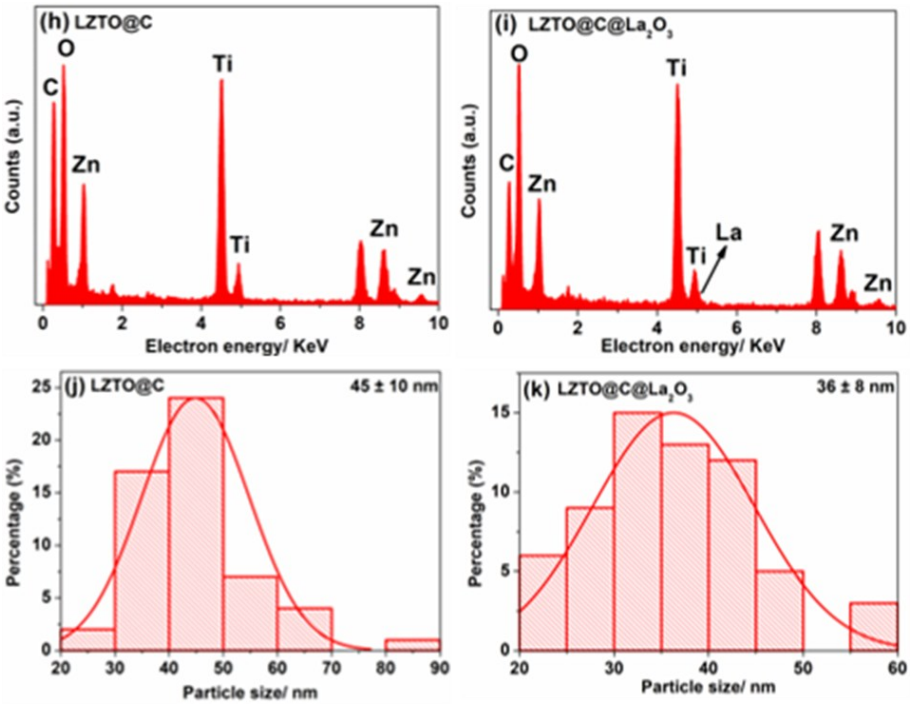

Fig. S3 (a) TEM image of LZTO@C@La_2O_3; Element mappings of (b) Zn, (c) Ti, (d) O, (e) C, (f) N and (g) La in LZTO@C@La_2O_3; Energy dispersive X-ray (EDX) spectroscopies of (h) LZTO@C and (i) LZTO@C@La_2O_3; Histograms of particle size distribution of (j) LZTO@C and (k) LZTO@C@La_2O_3.

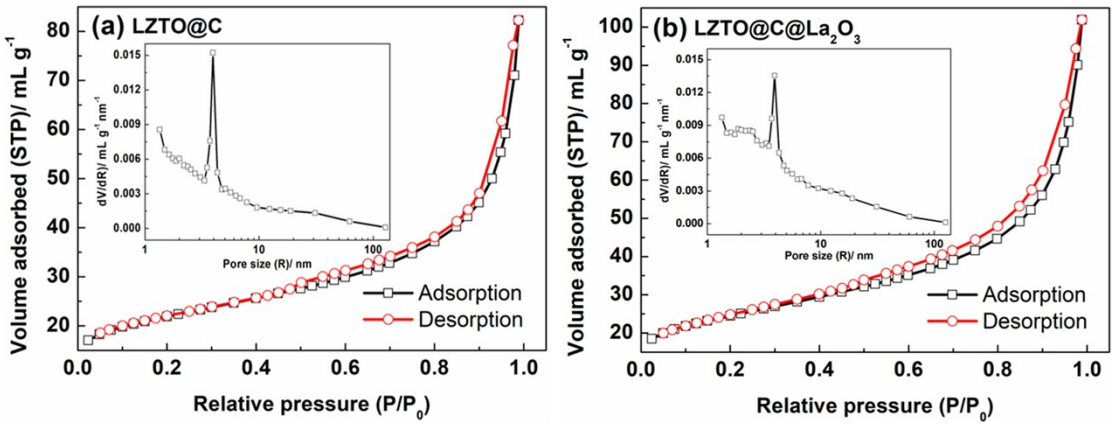

Fig. S4 N_2 adsorption-desorption isotherms of (a) LZTO@C and (b) LZTO@C@La_2O_3 (insets, the pore size distributions of the LZTO@C and LZTO@C@La_2O_3 anode materials).

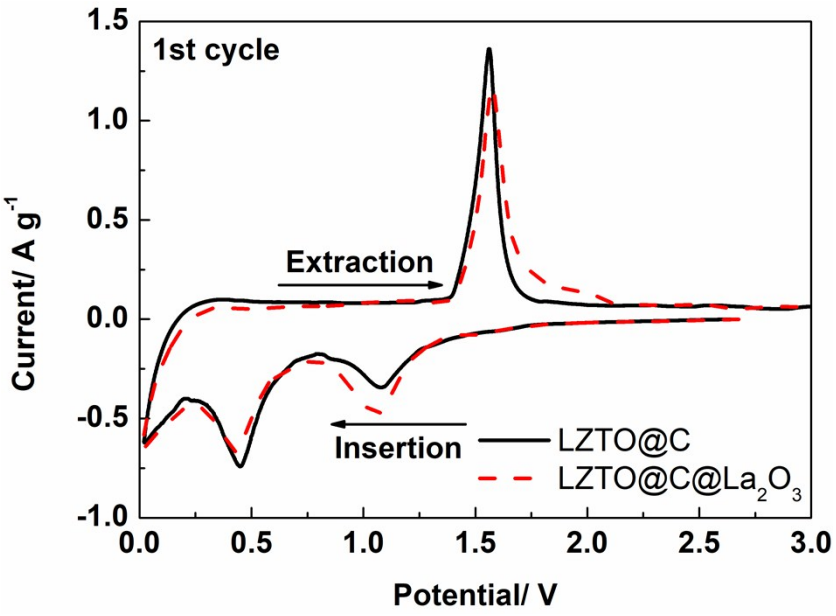

Fig. S5 Cyclic voltammograms of LZTO@C and LZTO@C@La_2O_3 electrodes at the 1st cycle at a rate of 0.5 mV s^{-1} in the range of 0.02-3.0 V (vs. Li/Li^+).

The CV curves of LZTO@C and LZTO@C@La_2O_3 were recorded at 0.5 mV s^{-1} in the potential range of 0.02-3.0 V and are shown in Fig. S5. There is an anodic peak and two cathodic peaks on the curves for each sample, corresponding to the Ti^{4+}/Ti^{3+} redox couple. The difference between anodic and cathodic peak potentials (φ_p) is 0.483 and 0.519 V for LZTO@C and LZTO@C@La_2O_3 at the 1st cycle, respectively (Table S3). Compared with the LZTO@C electrode, the LZTO@C@La_2O_3 electrode has larger φ_p, indicating that the polarization is larger for the electrode at the 1st cycle.

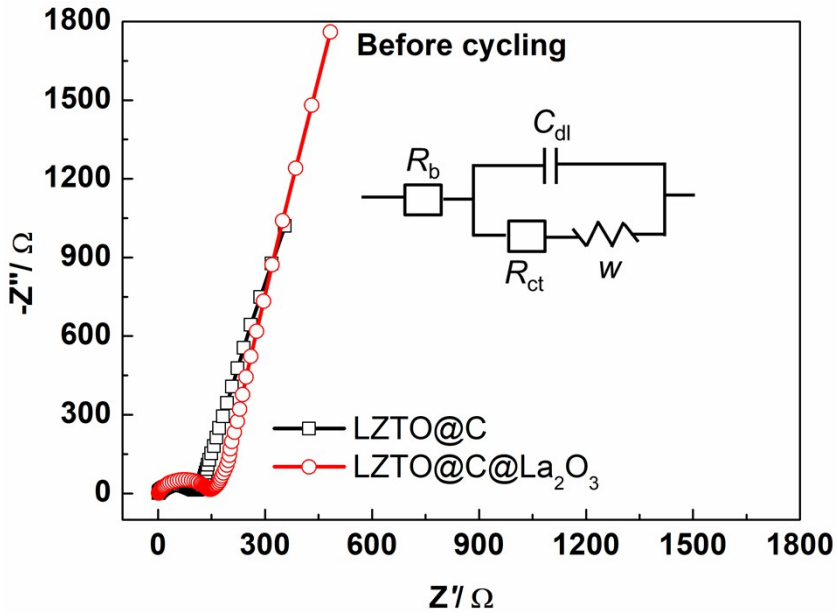

Fig. S6 Impedance spectra of LZTO@C and LZTO@C@La_2O_3 electrodes (inset, corresponding equivalent circuit).

For the LZTO@C and LZTO@C@La_2O_3 electrodes, the electrochemical impedance data were collected on as assembled cells before cycling and are presented in Fig. S6. The inset is the equivalent circuit model. R_b is the combined impedance of the electrolyte and cell components corresponding to the small intercept. C_{dl} and R_{ct} are the double layer capacitance and charge transfer resistance corresponding to the semicircle. W represents Warburg impedance. Compared with the LZTO@C electrode, the LZTO@C@La_2O_3 electrode has larger charge transfer resistance of 105.3 Ω (Table S4).

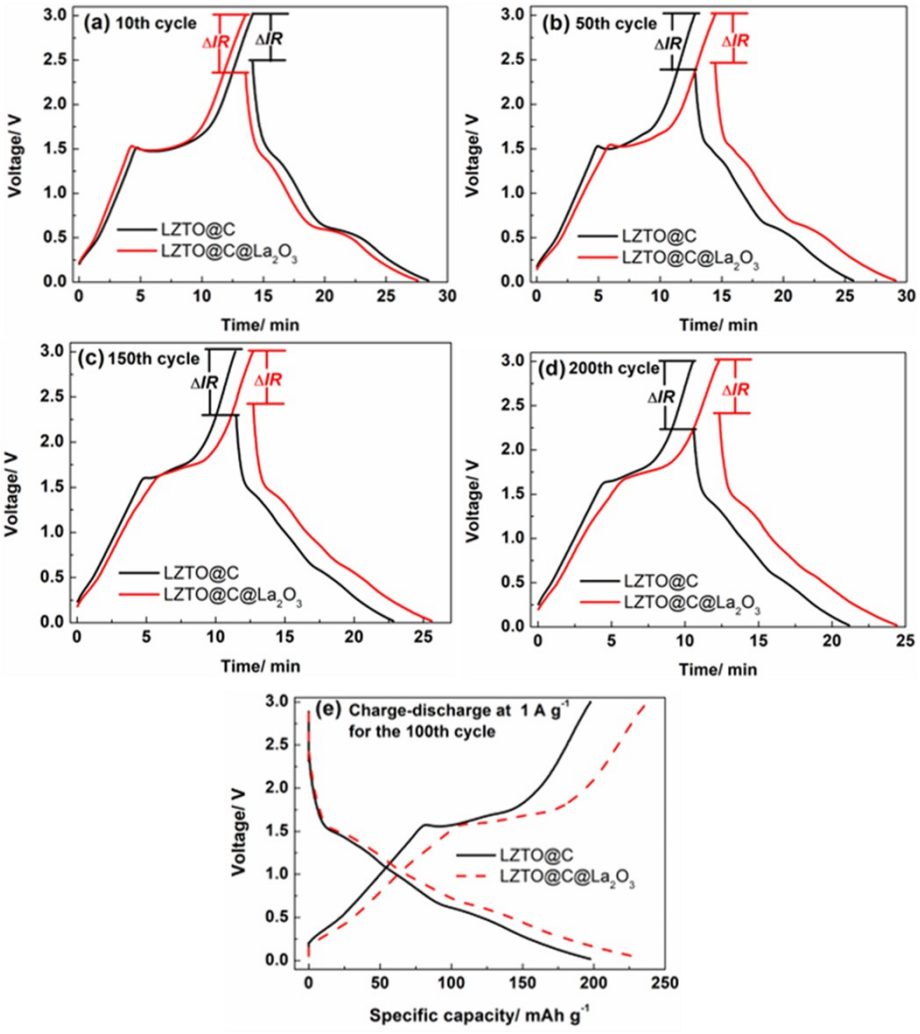

Fig. S7 IR-drop data of LZTO@C and LZTO@C@La_2O_3 electrodes at 1 A g^{-1} when charging is switched to discharging for the (a) 10th cycle, (b) 50th cycle, (c) 150th cycle and (d) 200th cycle; (e) Charge-discharge curves at the 100th cycle of LZTO@C and LZTO@C@La_2O_3 at 1 A g^{-1}.

The magnitude of internal resistance can be characterized by the voltage drop, or IR drop, when charging or discharging is switched to discharging or charging (Fig. S7a-d). The IR drop of LZTO@C is smaller than that of LZTO@C@La_2O_3 at the 10th cycle. However, the IR drop of LZTO@C is larger than that of LZTO@C@La_2O_3 in the subsequently cycling process.

Fig. S7e shows the charge-discharge curves of LZTO@C and LZTO@C@La_2O_3

at the 100th cycle. The potential difference between charge and corresponding discharge plateaus of LZTO@C@La_2O_3 is smaller than that of LZTO@C.

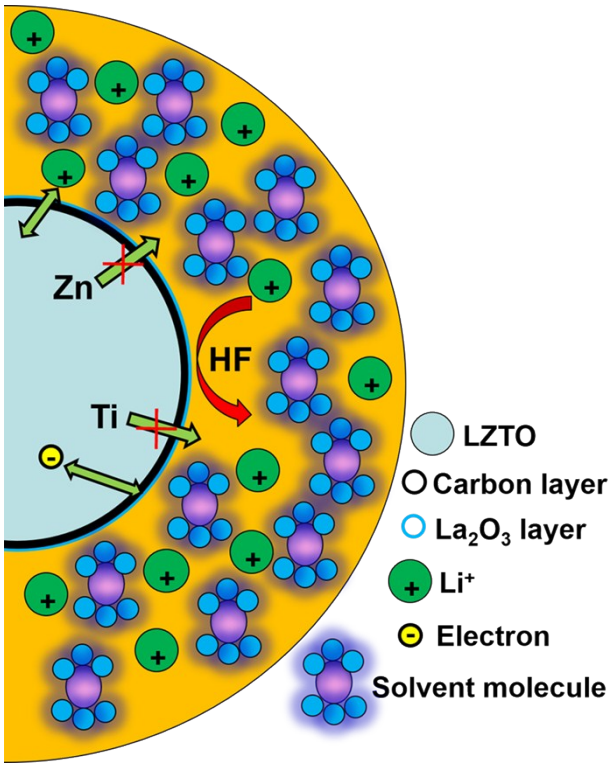

Fig. S8 Mechanism of the carbon and La_2O_3 co-coating layers preventing the dissolution of transition metal elements in the LZTO@C@La_2O_3 electrode.

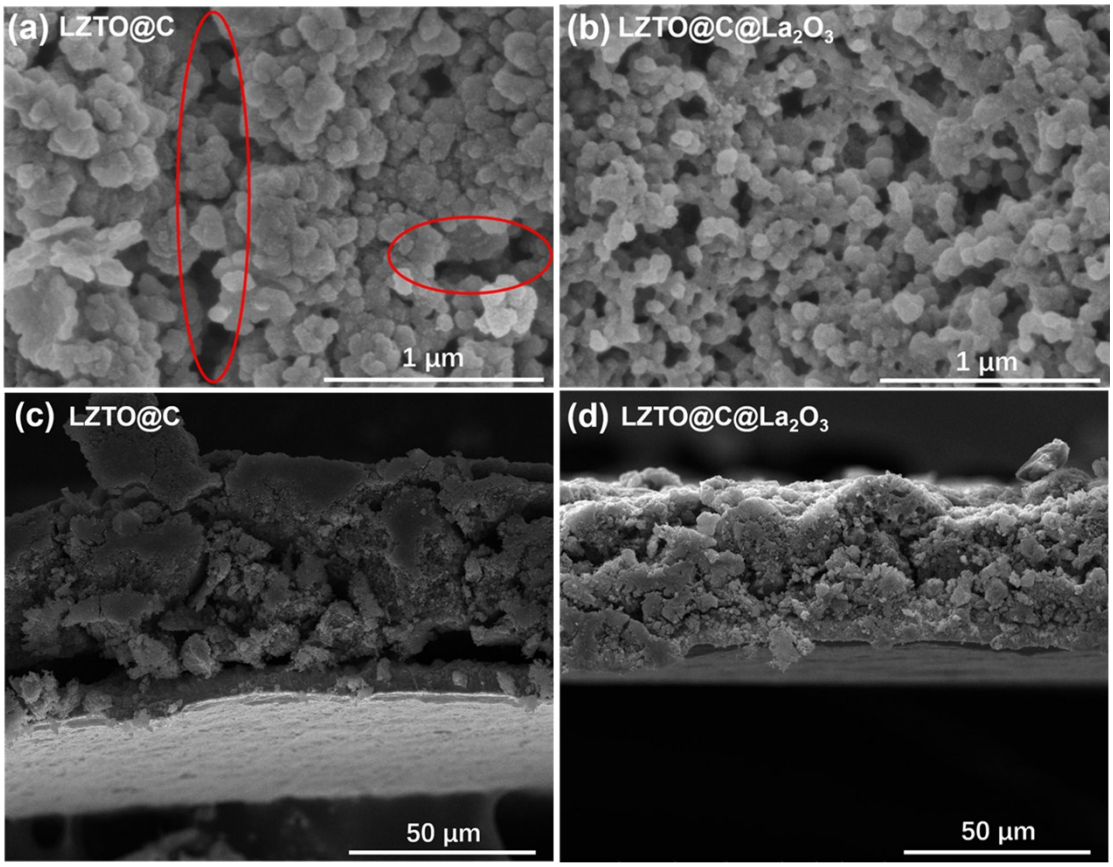

Fig. S9 Surface SEM images of (a) LZTO@C and (b) LZTO@C@La_2O_3 after cycling for 200 cycles at 1 A g^{-1}; Cross-sectional SEM images of (c) LZTO@C and (d) LZTO@C@La_2O_3 after cycling for 200 cycles at 1 A g^{-1}.

The SEM images of the LZTO@C and LZTO@C@La_2O_3 electrodes cycling for 200 cycles at 1 A g^{-1}, are shown in Fig. S9. The surface of the LZTO@C electrode is severely damaged after repeated Li^+ intercalation/deintercalation, and cracks with different width and depth appear (marked in red circles in Fig. S9a). The cracks will prevent the transportation of electrons and diffusion of Li^+ ions, and then lead to the capacity fading. However, there is no obvious crack on the surface of LZTO@C@La_2O_3 (Fig. S9b). From the cross-sectional SEM images as shown in Fig. S9c-d, compared with the LZTO@C electrode, the detachment of the active material layer from the Cu substrate is not pronounced for the LZTO@C@La_2O_3 electrode,

indicating the better adhesion between the active material layer and Cu current collector. This good adhesion helps to maintain a good electrical contact between the current collector and the active material.

Table S1 Lattice parameters of LZTO@C and LZTO@C@La_2O_3.

Samples	a (Å)	V (Å^3)
LZTO@C	8.373(4)	587.0(2)
LZTO@C@La_2O_3	8.373(7)	587.1(5)

Table S2 Specific surface areas, total pore volumes and average pore diameters of LZTO@C and LZTO@C@La_2O_3.

Samples	Specific surface area (m^2 g^{-1})	Total pore volume (mL g^{-1})	Average pore diameter (nm)
LZTO@C	58.3	0.116	7.1
LZTO@C@ La_2O_3	72.8	0.158	7.7

Table S3 Values of the CV peaks for LZTO@C and LZTO@C@La_2O_3 electrodes at the 1st cycle.

Samples	φ_{pa} (V)	φ_{pc} (V)	φ_p (V) = φ_{pa} - φ_{pc}
LZTO@C	1.566	1.083	0.483
LZTO@C@La_2O_3	1.578	1.059	0.519

Table S4 Impedance parameters calculated from equivalent circuit model.

Samples	R_b (Ω)	R_{ct} (Ω)
LZTO@C	2.467	70.69
LZTO@C@La_2O_3	2.415	105.3

Table S5 Electrochemical performance of LZTO in recent publications.

Material	Current density (A g^{-1})	2nd specific capacity (mAh g^{-1})	Cycle numbers	Capacity retention	Reference
$Li_2ZnTi_3O_8$	0.1	235	50	59.6%	[S2]
$Li_2Zn_{0.5}Cu_{0.5}Ti_3O_8$	0.1	240	50	67.5%	[S2]
$Li_2ZnTi_3O_8$+COS	1	195	200	81%	[S3]
$Li_2ZnTi_3O_8$+PVDF	1	160	200	38.8%	[S3]
LZTO-700-3	1	180.3	200	66.9%	[S4]
LZTO@C-700-1	1	236.5	200	60.8%	[S4]
LZTO@C-700-3	1	251.9	200	71.7%	[S4]
LZTO@C-700-5	1	245.7	200	69.7%	[S4]
LZTO-700-3	2	152.2	200	72.3%	[S4]
LZTO@C-700-1	2	182.8	200	67.2%	[S4]
LZTO@C-700-3	2	208.2	200	73.1%	[S4]
LZTO@C-700-5	2	207.8	200	65.7%	[S4]
LZTO@C-N-1	1	200.6	200	71.3%	[S5]
LZTO@C-N-2	1	207.9	200	77.7%	[S5]
LZTO@C-N-3	1	208.2	200	83.0%	[S5]
$Li_2ZnTi_3O_8/LiCoO_2$	2	175	200	68.6%	[S6]
$Li_2ZnTi_3O_8$	2	150	200	44.7%	[S6]
$Li_2ZnTi_3O_8$	3	170	200	44.1%	[S7]
$Li_2ZnTi_3O_8@Li_2MoO_4$	0.5/2	210	200	63.3%	[S8]
$Li_2ZnTi_3O_8@Li_2MoO_4$	0.5/3	190	200	74.7%	[S8]
$Li_2ZnTi_3O_8$/C@Cu	1	222	200	78.8%	[S9]
$Li_2ZnTi_3O_8$/C	1	220	200	65.5%	[S9]
$Li_2ZnTi_3O_8$/C@Cu	2	200	200	63.5%	[S9]
$Li_2ZnTi_3O_8$/C	2	198	200	53.5%	[S9]
$Li_2ZnTi_3O_8$/C@Cu	3	185	200	60.5%	[S9]
$Li_2ZnTi_3O_8$/C	3	170	200	58.8%	[S9]
LZTO@C@La_2O_3	1	233.4	200	89.8%	The work
LZTO@C@La_2O_3	2	230.2	200	77.2%	The work
LZTO@C@La_2O_3	3	210.6	200	76.7%	The work

Table S6 Rate capability of LZTO in recent publications.

Material	Current density (A g^{-1})	Specific capacity (mAh g^{-1})	Cycle numbers	Reference
LZTO@C-700-3	4	143.3	100	[S4]
LZTO@C-700-3	5	133.2	100	[S4]
LZTO@C-N-3	5	159.6	100	[S5]
$Li_2ZnTi_3O_8$	3	132.4	1	[S6]
$Li_2ZnTi_3O_8/LiCoO_2$	3	151.6	1	[S6]
$Li_2ZnTi_3O_8$	3	120	100	[S7]
$Li_2ZnTi_3O_8$/C	3	130	100	[S9]
$Li_2ZnTi_3O_8$/C@Cu	3	133	100	[S9]
$Li_2ZnTi_3O_8$	3	154	1	[S10]
$Li_2ZnTi_3O_8/La_2O_3$	3	148.2	1	[S10]
LZTO-2	5	101	51	[S11]
$Li_2ZnTi_3O_8$	3	125	100	[S12]
$Li_2ZnTi_3O_8/TiO_2$	3	162	100	[S12]
$Li_2ZnTi_3O_8$	3	113.3	100	[S13]
R-100-LZTO	5	94	100	[S14]
R-10-LZTO	5	55.6	100	[S14]
LZTO@C-N-700	4	123.4	80	[S15]
LZTO@C-N-700	5	115.3	80	[S15]
LZTO@C-N-2	3	177.3	100	[S16]
LZTO@C-N-2	5	159.7	100	[S16]
$Li_2ZnTi_3O_8$/C-2	3	160.5	100	[S17]
$Li_2ZnTi_3O_8$/C-2	4	139.7	100	[S17]
$Li_2ZnTi_3O_8$/C-2	5	129.1	100	[S17]
LZTO@C@La_2O_3	3	198.1	100	The work
LZTO@C@La_2O_3	4	174.3	100	The work
LZTO@C@La_2O_3	5	166.1	100	The work

References

S1 T. Ren, J.F. Zhang, D. Wang, P. Dong, J.G. Duan, X. Li, S. Rao, D.H. Huang, Y.J. Zhang, Enhancing the high-voltage performances of Ni-rich cathode materials by homogeneous La_2O_3 coating via a freeze-drying assisted method, Ceram. Int. 44 (2018) 14660-14666.

S2 W. Chen, H.F. Liang, W.J. Ren, L.Y. Shao, J. Shu, Z.C. Wang, Complex spinel titanate as an advanced anode material for rechargeable lithium-ion batteries, J. Alloys Compd. 611 (2014) 65-73.

S3 H.Q. Tang, Q. Weng, Z.Y. Tang, Chitosan oligosaccharides: A novel and efficient water soluble binder for lithium zinc titanate anode in lithium-ion batteries, Electrochim. Acta 151 (2015) 27-34.

S4 Z.H. Meng, L.J. Wang, X.X. Li, G.Q. Zhang, H.Y. Li, Synthesis of high performance carbon-coated lithium zinc titanate via an EDTA-assisted route, Int. J. Hydrogen Energy 42 (2017) 2177-2186.

S5 Z.H. Meng, X.F. Chen, L.J. Wang, F. Wang, Synthesis of high rate capability N-doped carbon coated on lithium zinc titanate via a surfactant-assisted solid-state route, RSC Adv. 7 (2017) 54258-54265.

S6 H.Q. Tang, J.T. Zhu, C.X. Ma, Z.Y. Tang, Lithium cobalt oxide coated lithium zinc titanate anode material with an enhanced high rate capability and long lifespan for lithium-ion batteries, Electrochim. Acta 144 (2014) 76-84.

S7 T. Liu, H.Q. Tang, L.L. Zan, Z.Y. Tang, Comparative study of $Li_2ZnTi_3O_8$ anode material with good high rate capacities prepared by solid state, molten salt and sol-gel methods, J. Electroanal. Chem. 771 (2016) 10-16.

S8 Z.F. Li, H. Li, Y.H. Cui, Z.G. Du, Y.H. Ma, C.X. Ma, Z.Y. Tang, Li_2MoO_4 modified $Li_2ZnTi_3O_8$ as a high property anode material for lithium ion battery, J. Alloys Compd. 692 (2017) 131-139.

S9 H.Q. Tang, Y.K. Zhou, L.L. Zan, N.Q. Zhao, Z.Y. Tang, Long cycle life of carbon

coated lithium zinc titanate using copper as conductive additive for lithium ion batteries, Electrochim. Acta 191 (2016) 887-894.

S10 H.Q. Tang, L.L. Zan, J.T. Zhu, Y.H. Ma, N.Q. Zhao, Z.Y. Tang, High rate capacity nanocomposite lanthanum oxide coated lithium zinc titanate anode for rechargeable lithium-ion battery, J. Alloys Compd. 667 (2016) 82-90.

S11 Y.R. Ren, P. Lu, X.B. Huang, J.N. Ding, H.Y. Wang, Synthesis and high cycle performance of $Li_2ZnTi_3O_8$/C anode material promoted by asphalt as a carbon precursor, RSC Adv. 6 (2016) 49298-49306.

S12 H. Li, Z.F. Li, Y.H. Cui, C.X. Ma, Z.Y. Tang, Long-cycled $Li_2ZnTi_3O_8/TiO_2$ composite anode material synthesized via a one-pot co-precipitation method for lithium ion batteries, New J. Chem. 41 (2017) 975-981.

S13 B.K. Chen, C.J. Du, Y.Z. Zhang, R.X. Sun, L. Zhou, L.J. Wang, A new strategy for synthesis of lithium zinc titanate as an anode material for lithium ion batteries, Electrochim. Acta 159 (2015) 102-110.

S14 L.J. Wang, Z.H. Meng, H.W. Wang, X.X. Li, G.Q. Zhang, Effects of TiO_2 starting materials on the synthesis of $Li_2ZnTi_3O_8$ for lithium ion battery anode, Ceram. Int. 42 (2016) 16872-16881.

S15 X.J. Wang, L.J. Wang, B.K. Chen, J. Yao, H.Y. Zeng, MOFs as reactant: In situ synthesis of $Li_2ZnTi_3O_8$@C-N nanocomposites as high performance anodes for lithium-ion batteries, J. Electroanal. Chem. 775 (2016) 311-319.

S16 Z.H. Meng, S. Wang, L. J. Wang, Synthesis of high performance N-doped carbon coated $Li_2ZnTi_3O_8$ via a NTA-assisted solid-state route, Dalton Trans. 47 (2018)

2711-2718.

S17 L.J. Wang, B.K. Chen, Z.H. Meng, B.M. Luo, X.J. Wang, Y.Y. Zhao, High performance carbon-coated lithium zinc titanate as an anode material for lithium-ion batteries, Electrochim. Acta 188 (2016) 135-144.